UNIVERSITÄT AUGSBURG
Universitätsbibliothek

OPEN ACCESS
OPUS AUGSBURG

Plasmonic wavelength-dependent optical switch

Deirdre Kilbane, Eva Prinz, Tobias Eul, Michael Hartelt, Anna-Katharina Mahro, Matthias Hensen, Walter Pfeiffer, Martin Aeschlimann

Angaben zur Veröffentlichung / Publication details:

Kilbane, Deirdre, Eva Prinz, Tobias Eul, Michael Hartelt, Anna-Katharina Mahro, Matthias Hensen, Walter Pfeiffer, and Martin Aeschlimann. 2023. "Plasmonic wavelength-dependent optical switch." *Optics Express* 31(6): 9579–90. https://doi.org/10.1364/oe.484035.

Nutzungsbedingungen / Terms of use:

CC BY 4.0

Dieses Dokument wird unter folgenden Bedingungen zur Verfügung gestellt: / This document is made available under these conditions:
CC-BY 4.0: Creative Commons: Namensnennung
Weitere Informationen finden Sie unter: / For more information see:
https://creativecommons.org/licenses/by/4.0/deed.de

Research Article Vol. 31, No. 6 / 13 Mar 2023 / Optics Express 9579
Optics EXPRESS

Plasmonic wavelength-dependent optical switch

DEIRDRE KILBANE,[1,*] EVA PRINZ,[2] TOBIAS EUL,[2] MICHAEL HARTELT,[2] ANNA-KATHARINA MAHRO,[2] MATTHIAS HENSEN,[3] WALTER PFEIFFER,[4] AND MARTIN AESCHLIMANN[2]

[1]*Walton Institute for Information and Communication Systems Science, South East Technological University, Waterford, Ireland*
[2]*Department of Physics and Research Center OPTIMAS, University of Kaiserslautern, Germany*
[3]*Institut für Physikalische und Theoretische Chemie, Universität Würzburg, Am Hubland, 97074 Würzburg, Germany*
[4]*Fakultät für Physik, Universität Bielefeld, Universitätsstraße 25, 33615 Bielefeld, Germany*
[*]*deirdre.kilbane@waltoninstitute.ie*

Abstract: We design and experimentally demonstrate an optical switch based on the interference of plasmonic modes in whispering gallery mode (WGM) antennas. Simultaneous excitation of even and odd WGM modes, enabled by a small symmetry breaking via non-normal illumination, allows switching the plasmonic near field between opposite sides of the antenna, depending on the excitation wavelength used in a wavelength range of 60 nm centered around 790 nm. This proposed switching mechanism is experimentally demonstrated by combining photoemission electron microscopy (PEEM) with a tunable wavelength femtosecond laser source in the visible and infrared.

Published by Optica Publishing Group under the terms of the Creative Commons Attribution 4.0 License. Further distribution of this work must maintain attribution to the author(s) and the published article's title, journal citation, and DOI.

1. Introduction

The field of plasmonics is concerned with achieving control over light-matter interaction on the nanometer spatial and femtosecond temporal scale. Understanding this interaction has led to the development of a range of novel technologies based on nano-optical components including ultrafast switching devices [1], tunable lasers [2], miniaturized biosensors with single molecule sensitivity [3], high-performance solar cells using energy-harvesting [4] as well as integrated photonic-plasmonic on-chip nanocircuitry [5–7]. Ultrafast optical switching components for integrated nanocircuitry require high speed, spectral tunability and small size [1,8–10]. Gold and silver nanostructures are ideal candidates since localised surface plasmon oscillations have a lifetime of approx. 10 fs [11] and a broad spectral response [12–14]. However, many of these optical switching devices rely on complicated fabrication procedures including multiple heterogeneous layers and high-order nonlinear effects. One example is a single Au/GeSbTe/Au nanosandwich structure that demonstrated localized surface plasmon resonance (LSPR) switching [8]. A GeSbTe layer acts as an active phase-change medium between a Au nanorod (AuNR) and a Au film. The phase change significantly alters the scattering intensity of the hybridized modes of the AuNR and Au film. Nonlinear plasmonic antennas serve as another example of an ultrafast optical switch [15]. The narrow gap between two metal nanorods was filled with semiconductive amorphous silicon (aSi) that acts as a photoconductive switch. In the unswitched case, i.e., aSi in the nonconductive state, the antenna supports half wavelength resonances over individual arms. In the switched case, i.e., with aSi in the conducting state, the half-wave modes hybridize due to a coupling of the antenna arms leading to a half-wave resonance over the full antenna length. This switching results in a shift in the spectral resonance position over 350 nm accompanied by a large change in the extinction ratio and a strong modification of the near-field intensity distribution.

#484035 https://doi.org/10.1364/OE.484035
Journal © 2023 Received 29 Dec 2022; revised 13 Feb 2023; accepted 13 Feb 2023; published 28 Feb 2023

Optics EXPRESS

Other examples include plasmonic indium tin oxide (ITO) nanorod arrays for infrared high-speed all-optical switching [9] and on-chip all-optical switching based on plasmon-photon hybrid nanostructures [10].

Here we aim to reduce the complexity of switching devices and design a wavelength-dependent optical switch in a single whispering gallery mode (WGM) antenna milled into a gold surface on a silicon substrate. Switching of the antenna-associated near field distribution maximum from one side of the antenna to the other simply relies on changing the excitation wavelength. Such a device could be readily incorporated into existing plasmonic nanocircuitry to extend its functionality. For example, it could be combined with or replace plasmonic Y-splitter/directional couplers which are used to route light emission to one of two output ports depending on the polarization of the light illuminating the input port [16]. In contrast, the WGM antenna switch can be used to route light in a particular direction by changing solely the polarization of the incident light which was demonstrated with PEEM [17]. WGM antennae have shown enormous potential as nanoscale components in a wide range of applications to date. WGM cavities consist of a circular groove ring resonator in a plane metal surface and function as an optical antenna. The groove supports circulating surface plasmon polaritons (SPPs) confined between the groove walls [18–21]. These form a standing wave pattern along the circumference resulting in whispering gallery resonances. The resonances are tunable through the radius of the ring and the depth of the groove. The WGM resonance modes (m) occur when the circumference of the ring equals an integer number of plasmon wavelengths. The lowest order azimuthal resonance, a dipolar resonance ($m = 1$), has two nodes and occurs if the ring circumference equals a single plasmon wavelength [18]. A quadrupolar mode ($m = 2$) has four nodes etc. Symmetry breaking introduced by non-normal angles of incidence allows us to simultaneously excite modes of different m that would not be excited under normal incidence conditions. Increasing the ring diameter results in higher-order azimuthal resonances, such as quadrupolar resonances. Additionally, increasing the groove depth results in higher-order radial modes due to an increase in the number of antinodes confined in the cavity groove [22,23].

Investigating the optical response of plasmonic structures such as WGMs is challenging due to the requirement of sub-diffraction limit imaging systems. PEEM allows us to directly determine the local near field of nanostructures. PEEM imaging of bowtie antennas demonstrated that phase-sensitive superposition of different plasmonic modes leads to a spatially controllable enhancement of the near-field inside and around the nanostructure [24]. This is also the control mechanism in polarization control of near-field localization demonstrated in WGMs under illumination centered at a single wavelength [17]. In [25,26] PEEM was combined with a wavelength tunable femtosecond laser source. This adds an additional degree of freedom [27], which is exploited here to demonstrate electromagnetic field localization in a WGM antenna. In [17] a detailed analysis was performed of the multi-modal response of an optical antenna, which consisted of a circular groove milled in a gold film on a dielectric ITO substrate. Superpositions of planar surface plasmon polariton modes (including dipole and quadrupole) resulted in odd and even numbers of nodes. Here we combine the concept of plasmonic modal interference with a small angle of incidence to introduce asymmetry which allows us to excite WGM modes with odd and even numbers of nodes and to thus control the spatial switching of the near-field distribution from L region to R region with increasing wavelength. This will advance applications in the miniaturization of optical switching devices such as routing in integrated plasmonic nanocircuitry design for optical fiber communication networks and in quantum information processing, and plasmonic nano biosensing with single molecule sensitivity.

The paper is organized as follows: First FDTD based simulations are performed to design a wavelength-dependent optical switch. Next the origin of the spatial switching of the near-field intensity is explained in terms of plasmonic modal interference. Finally, the experimental demonstration is presented, including details of the sample fabrication and PEEM imaging.

Optics EXPRESS

2. Design of a wavelength-dependent optical switch

Figure 1(a) shows a sketch of the WGM antenna switch design. The structure is a single nanoantenna milled into a thin gold surface on a silicon substrate. To aid our design of a plasmonic wavelength-dependent optical switch, finite-difference time-domain (FDTD) simulations were performed with the commercial software Lumerical (ANSYS Lumerical Software ULC, Vancouver, Canada, Finite Difference IDE R2.5 2021, Version 8.26.2885) based on the data of Johnson and Christy [28]. A p-polarized light pulse under an incidence angle of 5° generated by a broadband plane wave source with a temporal full-width at half maximum of ~4 fs and center wavelength of $\lambda = 800$ nm excites plasmonic WGMs, which result in an enhanced near-field intensity distribution at the top of the WGM groove. The simulations were performed on a uniformly-spaced grid with a maximum resolution of 2 nm in the antenna region. Outside the antenna region the mesh size is increased to 18 points per wavelength, depending on the refractive index of the respective material.

Figure 1(b) shows the simulated absorption spectrum (solid line) for an antenna of radius 300 nm and groove depth 150 nm. The broad absorption peak observed at 923 nm is due to the laser-excited resonant dipole mode. Figure 1. (c) shows the simulated near-field intensity distribution in a plane 10 nm below the Au surface on a logarithmic scale, $\log_{10}|E|^2$, at excitation wavelengths of 1101 nm, 923 nm, and 761 nm. At an excitation wavelength of 923 nm the dipole mode is clearly visible in the near-field distribution. At a shorter wavelength of 761 nm, the near-field intensity is mainly located at the left side of the groove while at a longer wavelength of 1101 nm it is mainly located at the right side of the groove.

The wavelength-dependent multiphoton PEEM yield polarization $P(\lambda)$ is a measure of the spatial switching of this near-field intensity distribution and it is calculated according to

$$P(\lambda) = \frac{Y_L(\lambda) - Y_R(\lambda)}{Y_L(\lambda) + Y_R(\lambda)}, \tag{1}$$

where $Y_L(\lambda)$ and $Y_R(\lambda)$ is the photoelectron emission yield calculated in the left (L) and right (R) half of a plane that is located 10 nm below the surface with its center in the middle of the antenna. For every wavelength λ of the laser spectrum, the N-th power of the near-field intensity distribution $I(\lambda)$ is added up in the L and R region giving $Y_L(\lambda)$ and $Y_R(\lambda)$, respectively, where N is the minimum number N of absorbed photons required for photoemission, i.e., to overcome the work function in a multiphoton electron emission process starting from an initial state at the Fermi level. Note that for a fixed work function value N changes with photon wavelength. Figure 1(b) shows the PEEM yield polarization $P(\lambda)$ as a function of wavelength for a work-function of 5 eV (dashed line) and 3 eV (dashed-dotted line), where the former value refers to gold as material and the latter value considers a reduction of the work-function by deposition of cesium. As expected from the observed switching of near-field intensity, the PEEM yield polarization changes sign around the dipolar resonance of the WGM antenna. Moreover, an almost complete yield polarization can be observed at wavelengths of 760 nm and 1100 nm.

FDTD simulations with local dipole sources allow identifying the modal interference that leads to the PEEM yield polarization in the present case of WGM antennas. Specifically, two pulsed dipole sources, with the same spectral parameters as the plane wave source, were positioned 10 nm centrally above the groove on opposing antenna sides. Depending on the relative phase of the dipole sources specific modes of the WGM antenna can be excited (Fig. 2. (a)): For zero relative phase we observe the dipolar ($m = 1$) and hexapolar ($m = 3$) mode at a wavelength of 906 nm and 669 nm, respectively, while for a relative phase of π we observe a monopolar ($m = 0$) and quadrupolar ($m = 2$) mode at 1082 nm and 763 nm, respectively. The spectral resonances of these modes are shown in Fig. 2(b) as an absorption spectrum for the case of excitation with symmetric dipoles (zero relative phase) and antisymmetric dipoles (relative phase of π).

Optics EXPRESS

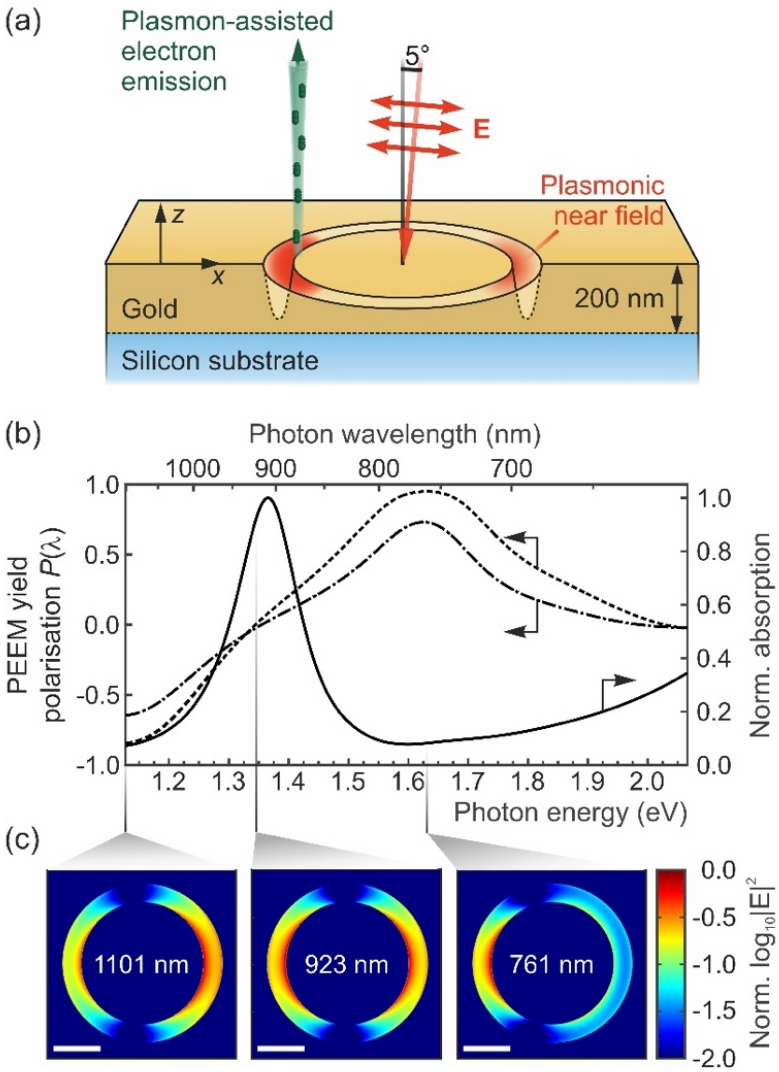


Fig. 1. (a) Schematic cross section of the ultrafast optical switch consisting of a single WGM nanoantenna milled into a thin gold surface on a silicon substrate. Light excites plasmonic modes in the groove resulting in a enhanced near-field intensity distribution. (b) Simulated multiphoton PEEM yield polarization, for a work function of 5 eV (dashed line) and 3 eV (dashed-dotted line), according to Eq. (1) and normalized absorption spectrum (solid line) for a single WGM antenna of radius $r = 300$ nm and groove depth $d = 150$ nm. To simplify the PEEM yield polarization calculation, all pixels in the left and right half of the WGM antenna contribute to the calculation of the respective PEEM yield, even if the near fields are inside the groove. (c) Simulated near-field intensity distribution $|E|^2$ on a logarithmic scale at wavelengths of 1101 nm, 923 nm and 761 nm. The corresponding field monitor is located 10 nm below the Au surface. The pulsed plane wave source ($\lambda = 800$ nm, 4 fs pulse duration) illuminates the antenna structure at an incidence angle of 5° and is p-polarized. Scale bars indicate a length of 200 nm.

Optics EXPRESS

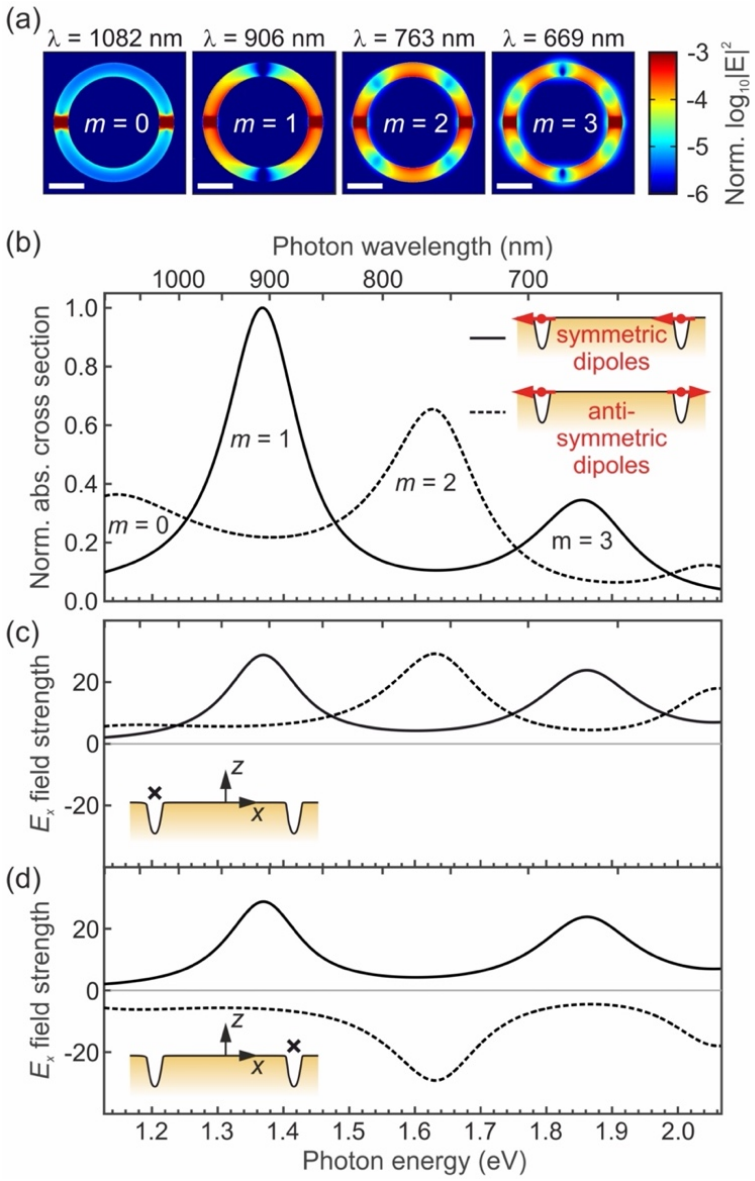


Fig. 2. (a) Simulated and $\log_{10}$-scaled near-field intensity distributions reveal different WGM antenna modes ranging from $m = 0$ to $m = 3$ at wavelengths of 1082 nm, 906 nm, 763 nm, and 669 nm, respectively. The modes $m = 0$ and $m = 2$ are excited by two pulsed dipole sources ($\lambda = 800$ nm, 4 fs pulse duration), which are located at opposite groove sides 10 nm above the Au surface, oscillating 180° out-of-phase. For the modes $m = 1$ and $m = 3$ the relative phase between the dipole sources was set to zero. Scale bars indicate a length of 200 nm. (b) Normalized absorption spectrum, i.e., the radiated dipole power which is absorbed by the nanostructure, for the excitation of the WGM antenna with the two dipole sources oscillating in-phase (solid line) and 180° out of phase (dashed line). (c) Electric field strength in the x-direction above the left WGM antenna groove. The dipole mode and quadrupole mode are in phase. (d) Electric field strength in the x-direction above the right WGM antenna groove. The dipole mode and quadrupole mode are clearly 180° out of phase.

Optics EXPRESS

The switching of near-field intensity, or PEEM yield polarization, gets evident by comparing the electric near-field along the x-direction at the opposing sides of the antenna groove for the different modes. Here, we focus on the x-component of the electric field since it is the dominating contribution at the specific positions. At the left side of the groove all modes exhibit the same sign of the electric field (Fig. 2(c)) and hence add up constructively. However, on the right side of the groove the modes, excited by symmetric and anti-symmetric dipole sources, differ in electric field direction (Fig. 2(d)) and thus add up destructively. Under normal-incidence conditions of a plane-wave source only the dipolar mode ($m = 1$) can be excited and no mode interference will occur. By introducing an even small angle of incidence of the incident plane wave symmetry is broken and all modes ($m = 0, 1, 2, 3, \ldots$) can be excited. Although the excitation cross section of non-dipolar modes is usually small, as can be seen with view to the antenna absorption shown in Fig. 1(b), their contribution to the total field is comparable to that of the dipolar mode away from the dipole resonance. As a consequence, the PEEM polarization yield exhibits $P(\lambda) \approx 1$ at the spectral position of the quadrupole mode ($m = 2$) near $\lambda = 760$ nm. There, the near-field strength on the short-wavelength slope of the dipole resonance ($m = 1$) is sufficiently small so that on one side of the antenna there is almost complete destructive interference of the overlapping fields.

In the following, we will experimentally demonstrate wavelength-dependent optical switching with WGM antennas by performing PEEM experiments with an incidence angle of 5°, i.e., we deliberately break the symmetry of excitation to allow the interference of near-field distributions of different modes.

3. Sample fabrication and characterization

To experimentally verify the proposed wavelength-dependent switching we fabricated arrays of WGM antennas of varying parameters (radius and depth) in gold as shown in Fig. 3(a). A smooth Au surface was obtained by thermal evaporation of a 200 nm thick Au layer onto a silicon wafer. Focused-ion-bean (FIB) milling with a 30 keV Ga beam was used to create the V-shaped grooves of the WGM antennas in the Au film. The WGM range of the ring radius (r) was 50–350 nm (step 25 nm), and the ring depth (d) was 60 nm, 100–180 nm (step 10 nm), and 200 nm. The width of the ring groove at the top was approximately 100 nm. The groove depth and radius were varied

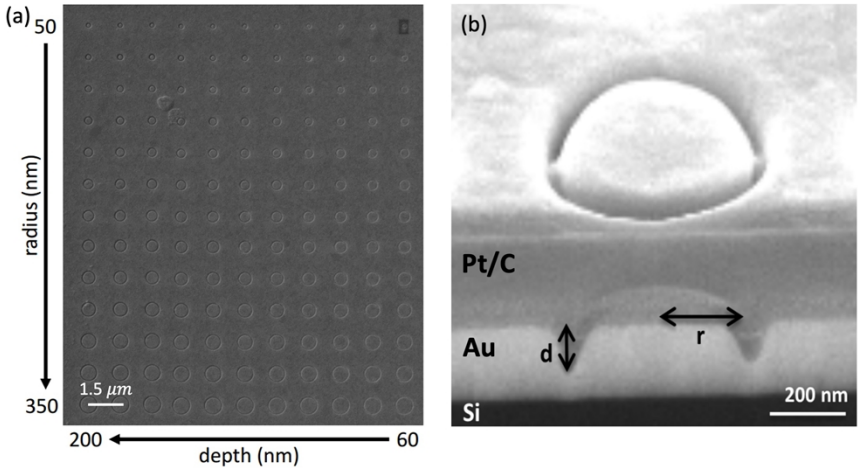


Fig. 3. (a) Scanning electron microscope (SEM) image of an array of a whispering gallery mode (WGM) antennas, (b) SEM image of the cross section of a single WGM antenna imaged at 52°, showing the high quality of the fabrication. To allow measuring the depth of the antenna, a layer of 20% Pt and 80% C was deposited on top of the Au.

Optics EXPRESS

systematically as shown in the scanning electron microscope image (SEM) in Fig. 3(a), with r increasing from top to bottom and d increasing from right to left. A typical SEM image of an individual WGM antenna is shown in Fig. 3. (b) and highlights the high-quality fabrication process, particularly the uniform surface and well-defined V-grooves. This quality is consistent throughout the samples used in this study. Several arrays were prepared on the same sample to test for the reproducibility of results. These were positioned far enough away to avoid any unwanted diffraction effects.

4. Photoemission electron microscopy

Photoemission electron microscopy was used to image the near-field distribution of arrays of WGM nanoantennas at various wavelengths. The PEEM used in our experiments is a NI-IS-PEEM (Focus GmbH) that operates in ultra-high vacuum with a spatial resolution better than 40 nm. A small mirror located at the back focal plane of the objective allows illuminating a sample in the PEEM at a small angle of incidence of 5° as shown in the schematic diagram in Fig. 4 (a). This mode of operation referred to as near normal incidence (nNI) geometry is used throughout this study. UV light from a mercury lamp was used to characterize the shape of the nanoantennas in single-photon PEEM. A femtosecond laser excites plasmons in nanostructures milled into the surface of gold and the emitted photoelectrons are recorded by the CCD camera of the PEEM. A sub-monolayer of cesium is evaporated onto the gold sample prior to imaging to reduce the work function of the noble metal. This leads to the emission of the electrons in a two-photon photoemission (2PPE) process with three-photon photoemission (3PPE) contribution also possible. This was experimentally confirmed by power law measurements, i.e., recording the photoelectron yield as a function of laser power. Due to its nonlinearity, 2PPE is highly sensitive to the local near-field. PEEM is therefore a very sensitive technique to measure small variations in the electric field distribution near the surface of gold which makes it highly suitable for imaging plasmonic modes excited in nanostructures [29].

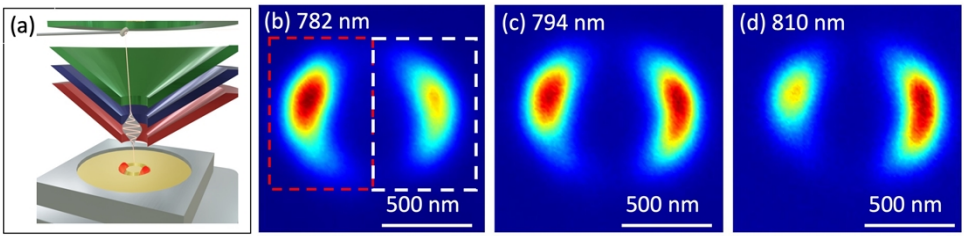


Fig. 4. (a) Schematic of single whispering gallery mode (WGM) antenna excited by incident light and photoemission electron microscope (PEEM) for recording the near field distribution. PEEM images of a whispering gallery mode (WGM) antenna with radius 325 nm and depth 150 nm at various wavelengths. The red (white) dashed box indicates the region of interest (ROI) used for integrating yield on the left (right). Near-field photoelectron emission distribution at wavelengths (b) 782 nm, (c) 794 nm, and (d) 810 nm.

PEEM images were recorded for a range of individual wavelengths under uniform illumination conditions including polarization, laser power, beam size, and beam shape. Here a wavelength tunable Ti:sapphire femtosecond laser (SPECTRA Physics MaiTai) was used, with a wavelength range of 720 –1040 nm, a pulse duration of 80 fs at a repetition rate of 80 MHz. The output power was maintained at ~100 ± 1 mW for each wavelength to ensure the detector was never saturated throughout measurements. The measurements presented in this study are for p-polarized light. And the array of WGM antennas is uniformly illuminated by the focused laser beam. Various properties of the WGM antennas can be systematically investigated by integrating the near-field

Optics EXPRESS

intensity over the entire sample or a specific region of interest (ROI) as described in detail in the next section.

Near field images of the WGM antenna arrays were recorded using the PEEM at wavelengths between 720–850 nm in 2 nm steps. Exemplary PEEM images showing the near-field photoelectron emission distribution for a WGM antenna with radius r = 325 nm and depth d = 150 nm are shown in Fig. 4. (b) – (d). A clear spatial switching in the x-direction (from left to right) of the near-field photoelectron distribution is observed when the wavelength (color) of the laser is changed from (a) 782 nm (left) through (b) 794 nm to (c) 810 nm (right). This spatial switching is most pronounced for the WGM antenna shown but is also observed for other WGM antennas with various combinations of radius and depth.

5. Near-field spectra

To quantify the wavelength-dependent changes in the near-field distribution, the total two-photon PEEM yield per WGM antenna was calculated by summing the pixel values for a ROI of 100×80 pixels centered at an individual WGM antenna. The normalized yield (yield norm.) was obtained by dividing this total wavelength-dependent yield by the maximum yield. PEEM images were recorded at each wavelength three times and averaged accordingly. Figure 5 shows the so obtained normalized near-field PEEM yield spectra (blue solid line) for four different WGM antennas. Next, the experimental PEEM yield polarization between the left (L) and right (R) part of the WGM nanoantenna (orange solid line) was quantified by applying the procedure based on Eq. (1) to the wavelength-dependent PEEM images with the ROIs for L and R emission as defined in Fig. 4(b). A clear transition of the near-field distribution from left to right is observed in the PEEM yield polarization shown in Fig. 5 as could already be assumed from the near-field images shown in Fig. 4(b) – (d) at a wavelength of (b) 782 nm, (c) 794 nm, and (d) 810 nm. Note that the lower switching contrast of only about 20% is attributed to the fact that in the experiment the emission is dominated by a two-photon electron emission process whereas the theoretically predicted contrast of almost 100% is based on a $N \approx 4$ process (work function of 5 eV), which enhances the contrast. As shown in Fig. 1 (b), a reduction of the work function leads to a reduction of polarization contrast.

The theoretical explanation for the switching can be inferred from a combination of the experiments and simulations performed on the WGM antenna array. At a wavelength of 782 nm, there is a noticeable interference between the dipole mode ($m = 1$) and the quadrupole mode ($m = 2$) which are in phase along the in-plane direction of the light polarization. This results in the near-field intensity distribution shifting to the left of the WGM nanoantenna as shown in Fig. 1 (c). In contrast at a wavelength of 810 nm, the long-wavelength region, there is also a noticeable interference between the dipole mode ($m = 1$) and the monopole mode ($m = 0$) which results in the PEEM yield distribution, i.e., the near-field intensity, shifting to the right of the nanoantenna, as shown in Fig. 4 (d). Therefore, the origin of the spatial switching effect can be attributed to a Fano resonance and plasmonic modal interference already at a small angle of incidence. The Fano resonance results from interference of the dipole mode ($m = 1$) and the quadrupolar mode ($m = 2$) as shown in Fig. 2 (b). Previously such effects were only observed at large incidence angles of 65° [23]. Employing smaller angles of incidence paves the way for more compact designs of ultrafast optical switches for use in miniaturized devices.

For the sensitivity of an optical switch as presented here, it is helpful if the switching process takes place on very small wavelength scales. By looking at the measured PEEM yield polarization curves in Fig. 5. (orange solid line) it can be inferred that switching of the corresponding near-field intensity distribution takes place on a scale of 50 nm. In contrast, the simulation of the WGM antenna in Fig. 1 reveals a switching process on much larger scales, i.e., more than 200 nm. We attribute this discrepancy of experiment and simulation to the influence of the array structure on the near-field patterns. In particular, plasmonic lattice resonances can interact with

Optics EXPRESS

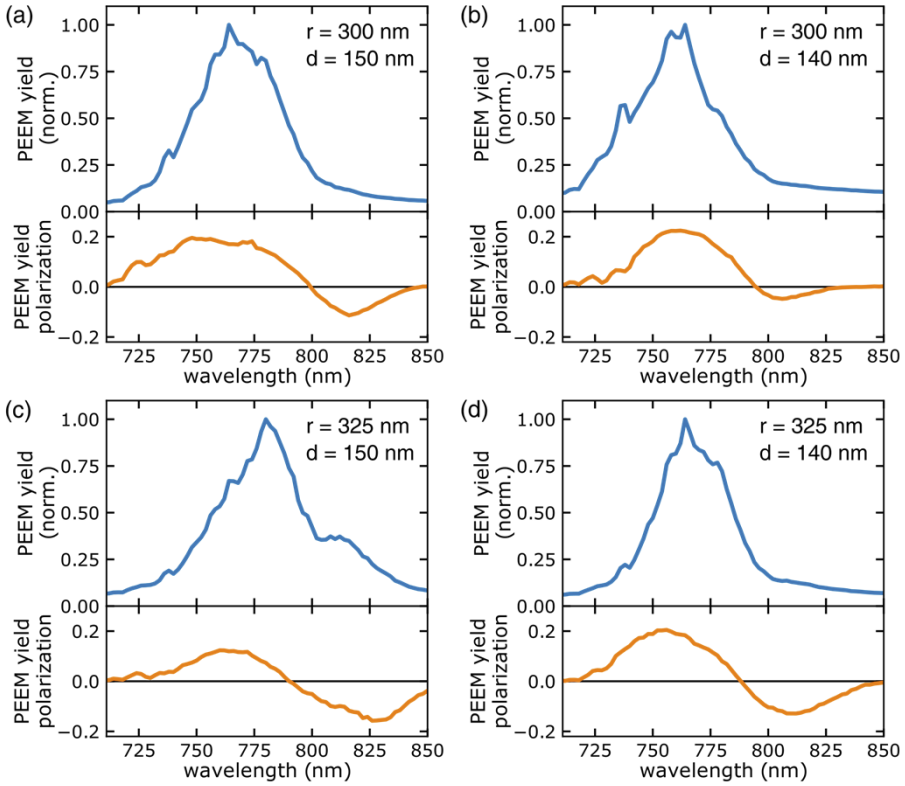


Fig. 5. Normalized near-field PEEM yield spectra (blue) and PEEM yield polarization (orange) for whispering gallery mode antenna of (radius, depth), (a) (300 nm, 150 nm), (b) (300 nm, 140 nm), (c) (325 nm, 150 nm), and (d) (325 nm, 140 nm).

the response of the individual WGM antennas to produce a more complicated local response. Plasmon lattice modes originate from the fact that a periodic pattern of antennas is written as shown in the SEM image in Fig. 3 (a): WGM modes could interact with grating-coupled SPPs on the flat metal surface and if the separation between neighbouring antennas is chosen so that coherent coupling between antennas results and lattice plasmon resonances occur. Since rather small distances between neighbouring WGM antennas were chosen we cannot exclude the appearance of such resonances. The detailed analysis of the influence of the antenna grid on the individual antenna response is beyond the scope of this work but we note that there is a noticeable increase in switching sensitivity when using arrays of WGM antennas instead of individual nanostructures.

6. Outlook

Plasmonics forms a natural interface between electronics and photonics for developing large-scale on-chip integrated photonic-plasmonic systems [4–7]. For example, plasmonic nanostructures can be used as micro lasers in plasmonic circuits for high-speed manipulation of optical information with minimal heat dissipation [5]. WGM resonators were designed to control light-matter interactions and strong spontaneous emission of a local emitter based on their geometry over a broad spectral range [18]. Now at the dawn of the quantum internet era, WGM antennas also show great potential. Aeschlimann et al. demonstrated strong coupling of optical nanoantennas placed at the foci of an elliptical plasmonic cavity [30]. This resulted in cavity-assisted ultrafast

Optics EXPRESS

long-range periodic energy transfer between plasmonic antennas. Subsequently, Hensen et al. showed theoretically that two quantum emitters, separated by 1.8 μm are strongly coupled via the delocalized plasmon mode with a high degree of entanglement [31]. This is very promising for applications in optical communication and quantum information processing where WGM antennas could potentially be used to couple single emitters to quantum plasmonic circuits in complex quantum communication networks. Pulse shaping [32] could also be used here to investigate the opportunity to create an ultrafast optical switch in real-time on the femtosecond timescale. In addition, plasmonics could play a crucial role in the development of quantum memories. One of the most promising candidates for quantum memories is single diamond color centers. Kumar et al. demonstrated efficient coupling of a single diamond color center to propagating plasmonic gap modes [33]. In addition, a quantum memory at telecom wavelengths has been developed based on nanofabricated mechanical resonators [34], and an efficient quantum microwave-to-optical converter has been achieved using electro-optic nanophotonic coupled resonators [35].

7. Conclusion

We designed a WGM antenna that functions as a wavelength-dependent optical switch that can be controlled by simply selecting the wavelength of the excitation source. Different wavelengths result in plasmonic modal interference that strikingly changes the near-field distribution to be located at the opposite side of the antenna. We used photoemission electron microscopy to image interfering near-field plasmonic modes. It is possible to increase the contrast between left and right and hence the overall switching effect by optimizing various parameters like the groove depth, radius, materials, and the incidence angle. In particular, the angle of incidence and the associated symmetry breaking could play an important role here to control the excitation ratio of the modes. This optimization will be the subject of future studies to advance applications in the miniaturization of optical switching devices, such as in routing in integrated plasmonic nanocircuitry design for optical fiber communication networks and in quantum information processing circuitry and plasmonic nano biosensing. Future research into WGM antennas as optical switches will focus on advancing the miniaturization of components for integrated hybrid photonic-plasmonic circuits. This will be achieved by investigating a combination of individual photonic and plasmonic components into more complex integrated logic circuits with ultrafast controllable functionalities. By a suitable choice of groove parameters, the optical switch can be designed to operate at a range of wavelengths depending on the application. Other noble materials that support plasmonics such as silver, copper, and aluminum will be investigated to improve CMOS compatibility.

Funding. Science Foundation Ireland (13/RC/2077_P2).

Acknowledgments. D. Kilbane acknowledges that this publication has emanated from research supported in part by a Grant from Science Foundation Ireland under Grant number 13/RC/2077_P2.

Disclosures. The authors declare no conflicts of interest.

Data availability. Data underlying the results presented in this paper are not publicly available at this time but may be obtained from the authors upon reasonable request.

References

1. X. Zhang and J. Yang, "Ultrafast plasmonic optical switching structures and devices," Front. Phys. **7**(190), 1–15 (2019).
2. A. Yang, T. B. Hoang, M. Dridi, C. Deeb, M. H. Mikkelsen, G. C. Schatz, and T. W. Odom, "Real-time tunable lasing from plasmonic nanocavity arrays," Nat. Commun. **6**(1), 6939 (2015).
3. F. Vollmer and A. Arnold, "Whispering-gallery-mode biosensing: label-free detection down to single molecules," Nat. Methods **5**(7), 591–596 (2008).
4. Y. S. Wang, M. Li, X. Zhou, P. Li, X. Hu, and Y. Song, "High efficient perovskite whispering-gallery solar cells," Nano Energy **51**, 556–562 (2018).

Optics EXPRESS

5. W. L. Barnes, A. Dereux, and T. W. Ebbessen, "Surface Plasmon subwavelength optics," Nature **424**(6950), 824–830 (2003).
6. E. Ozbay, "Plasmonics: Merging photonics and electronics at nanoscale dimensions," Science **311**(5758), 189–193 (2006).
7. Y. Fang and M. Sun, "Nanoplasmonic waveguides: towards applications in integrated nanophotonic circuits," Light: Sci. Appl. **4**(6), e294 (2015).
8. T. Hira, T. Homma, T. Uchiyama, K. Kuwamura, Y. Kihara, and T. Saiki, "All-optical switching off localized surface plasmon resonance in single gold nano sandwich using GeSbTe film as an active medium," Appl. Phys. Lett. **106**(3), 031105 (2015).
9. P. J. Guo, R. D. Schaller, J. B. Ketterson, and H.R. P. Chang, "Ultrafast switching of tunable infrared plasmons in indium tin oxide nanorod arrays with large absolute amplitude," Nat. Photonics **10**(4), 267–273 (2016).
10. Z. Chai, Y. Zhu, X. Hu, X. Yang, Z. Gong, F. Wang, H. Yang, and Q. Gong, "On-chip optical switch based on plasmon-photon hybrid nanostructure-coated multicomponent nanocomposite," Adv. Opt. Mater. **4**(8), 1159–1166 (2016).
11. M. Scharte, R. Porath, T. Ohms, M. Aeschlimann, J. R. Krenn, H. Ditlbacher, F. R. Aussenegg, and A. Liebsch, "Do Mie plasmons have a longer lifetime on resonance than off resonance?" Appl. Phys. B **73**(4), 305–310 (2001).
12. P. C. McPoli, N. Olivier, J.-S. Bouillard, D. O'Connor, A. V. Krasavin, W. Dickson, G. A. Wurtz, and A. V. Zayats, "Universal switching of plasmonic signals using optical resonator modes," Light: Sci. Appl. **6**(6), e16237 (2016).
13. K. D. Wang, I. Chen, H. J. Zhang, and J. Chen, "Controlling surface plasmon polaritons at femtosecond timescales on an aluminium-coated grating," Appl. Phys. Lett. **110**(2), 021105 (2017).
14. J. Kim, E. G. Carnemolla, C. DeVault, A. M. Shaltout, D. Faccio, V. M. Shalaev, A. V. Kildishev, M. Ferrera, and A. Boltasseva, "Dynamic control of nanocavities with tunable metal oxides," Nano Lett. **18**(2), 740–746 (2018).
15. N. Large, M. Abb, J. Aizpurua, and O. L. Muskens, "Photoconductively loaded plasmon nanoantenna as building block for ultracompact optical switches," Nano Lett. **10**(5), 1741–1746 (2010).
16. G. Razinskas, D. Kilbane, P. Melchior, P. Geisler, E. Krauss, S. Mathias, B. Hecht, and M. Aeschlimann, "Normal incidence PEEM imaging of propagating modes in a plasmonic nanocircuit," Nano Lett. **16**(11), 6832–6837 (2016).
17. R. C. Word, J. P. S. Fitzgerald, and R. Konenkamp, "Positional control of plasmonic fields and electron emission," Appl. Phys. Lett. **105**(11), 111114 (2014).
18. E. J. R. Vesseur, F. J. García de Abajo, G. , and A. Polman, "Modal decomposition of surface-plasmon whispering gallery resonators," Nano Lett. **9**(9), 3147–3150 (2009).
19. E. J. R. Vesseur, F. J. García de Abajo, and A. Polman, "Broadband Purcell enhancement in plasmonic ring cavities," Phys. Rev. B **82**(16), 165419 (2010).
20. S. I. Bozhevolnyi, V. S. Volkov, E. Devaux, and T. W. Ebbesen, "Channel plasmon-polariton guiding by subwavelength metal grooves," Phys. Rev. Lett. **95**(4), 046802 (2005).
21. C. L. C. Smith, N. Stenger, A. Kristensen, N. A. Mortensen, and S. I. Bozhevolnyi, "Gap and channeled plasmons in tapered grooves: a review," Nanoscale **7**(21), 9355–9386 (2015).
22. E. J. R. Vesseur and A. Polman, "Plasmonic whispering gallery cavities as optical antennas," Nano Lett. **11**(12), 5524–5530 (2011).
23. P. Melchior, D. Kilbane, E. J. Vesseur, A. Polman, and M. Aeschlimann, "Photoelectron imaging of modal interference in plasmonic whispering gallery cavities," Opt. Express **23**(25), 31619–31626 (2015).
24. P. Melchior, D. Bayer, C. Schneider, A. Fischer, M. Rohmer, W. Pfeiffer, and M Aeschlimann, "Optical near-field interference in the excitation of a bowtie antenna," Phys. Rev. B **83**(23), 235407 (2011).
25. H. Yu, Q. Sun, K. Ueno, T. Oshikiri, A. Kubo, Y. Matsuo, and H. Misawa, "Exploring coupled plasmonic nanostructures in the near field by photoemission electron microscopy," ACS Nano **10**(11), 10373–10381 (2016).
26. Q. Sun, H. Yu, K. Ueno, A. Kubo, Y. Matsuo, and H. Misawa, "Dissecting the few-femtosecond dephasing time of dipole and quadrupole modes in gold nanoparticles using polarized photoemission electron microscopy," ACS Nano **10**(3), 3835–3842 (2016).
27. T. Brixner, F. J. García de Abajo, J. Schneider, C. Spindler, and W. Pfeiffer, "Ultrafast Adaptive Optical Near-Field Control," Phys. Rev. B **73**(12), 125437 (2006).
28. P. B. Johnson and R. W. Christy, "Optical constants of the noble metals," Phys. Rev. B **6**(12), 4370–4379 (1972).
29. P. Kahl, S. Wall, C. Witt, C. Schneider, D. Bayer, A. Fischer, P. Melchior, M. Horn-von Hoegen, M. Aeschlimann, and F. J. Meyer zu Heringdorf, "Normal-incidence photoemission electron microscopy (NI-PEEM) for imaging surface plasmon polaritons," Plasmonics **9**(6), 1401–1407 (2014).
30. M. Aeschlimann, T. Brixner, M. Cinchetti, B. Frisch, B. Hecht, M. Hensen, B. Huber, C. Kramer, E. Krauss, T. H. Loeber, W. Pfeiffer, M. Piecuch, and P. Thielen, "Cavity-assisted ultrafast long-range periodic energy transfer between plasmonic antennas," Light: Sci. Appl. **6**(11), e17111 (2017).
31. M. Hensen, T. Heilpern, S. K. Gray, and W. Pfeiffer, "Strong coupling and entanglement of quantum emitters embedded in a nanoantenna-enhanced plasmonic cavity," ACS Photonics **5**(1), 240–248 (2018).
32. M. Aeschlimann, M. Bauer, D. Bayer, T. Brixner, S. Cunovic, F. Dimler, A. Fischer, W. Pfeiffer, M. Rohmer, C. Schneider, F. Steeb, C. Struber, and D. V. Voronine, "Spatiotemporal control of nanoptical excitations," Proc. Natl. Acad. Sci. U. S. A. **107**(12), 5329–5333 (2010).
33. S. Kumar, H. Alexander, and U. L. Andersen, "Efficient coupling of a single diamond color center to propagating plasmonic gap modes," Nano Lett. **13**(3), 1221–1225 (2013).

Optics EXPRESS

34. A. Wallucks, I. Markinović, B. Hensen, R. Stockill, and S. Gröblacher, "A quantum memory at telecom wavelengths," Nat. Phys. **16**(7), 772–777 (2020).
35. M. Soltani, M. Zhang, C. Ryan, G. J. Ribeill, C. Wang, and M. Loncar, "Efficient quantum microwave-to-optical conversion using electro-optic nanophotonic coupled resonators," Phys. Rev. A **96**(4), 043808 (2017).